Journal of Materials Science & Technology 122 (2022) 68–76

Contents lists available at ScienceDirect

Journal of Materials Science & Technology

journal homepage: www.elsevier.com/locate/jmst

Research Article

The influence of spark plasma sintering temperatures on the microstructure, hardness, and elastic modulus of the nanocrystalline Al-*x*V alloys produced by high-energy ball milling

J. Christudasjustus[a], C.S. Witharamage[a], Ganesh Walunj[b], T. Borkar[b], R.K. Gupta[a,*]

[a] Department of Materials Science and Engineering, North Carolina State University, Raleigh, NC 27606, United States
[b] Department of Mechanical Engineering, Cleveland State University, Cleveland, OH 44115, United States

ARTICLE INFO

Article history:
Received 28 November 2021
Revised 23 January 2022
Accepted 9 February 2022
Available online 19 March 2022

Keywords:
Spark plasma sintering
Aluminum alloys
Nanocrystalline alloys
High-energy ball milling
Nanoindentation
Hardness
Elastic modulus

ABSTRACT

Al-*x*V alloys (x = 2 at.%, 5 at.%, 10 at.%) with nanocrystalline structure and high solid solubility of V were produced in powder form by high-energy ball milling (HEBM). The alloy powders were consolidated by spark plasma sintering (SPS) employing a wide range of temperatures ranging from 200 to 400 °C. The microstructure and solid solubility of V in Al were investigated using X-ray diffraction analysis, scanning electron microscope and transmission electron microscope. The microstructure was influenced by the SPS temperature and V content of the alloy. The alloys exhibited high solid solubility of V–six orders of magnitude higher than that in equilibrium state and grain size < 50 nm at all the SPS temperatures. The formation of Al_3V intermetallic was detected at 400 °C. Formation of a V-lean phase and bimodal grain size was observed during SPS, which increased with the increase in SPS temperature. The hardness and elastic modulus, measured using nanoindentation, were significantly higher than commercial alloys. For example, Al-V alloy produced by SPS at 200 °C exhibited a hardness of 5.21 GPa along with elastic modulus of 96.21 GPa. The evolution of the microstructure and hardness with SPS temperatures has been discussed.

1. Introduction

Aluminum (Al) alloys have emerged as an effective structural material due to their high strength-to-weight ratio and a wide range of useful properties [1,2]. Precipitation strengthening has been the main strengthening mechanism for high strength Al alloys where size and volume fraction of precipitates along with the distance between adjacent precipitates dictate the strength. These precipitates cause the inevitable localized corrosion by galvanic interaction with reactive Al matrix which escalates with increasing volume fraction and size of the precipitates [3,4]. Therefore, the commercial Al alloys produced by conventional ingot metallurgy show a tradeoff between corrosion performance and mechanical properties [5], and consequently alternate strengthening mechanisms that could either increase corrosion resistance or do not affect corrosion [6–8].

Solid solution strengthening with suitable alloying elements and grain refinement has shown to increase corrosion resistance and strength simultaneously [6,7,9–11]. Several non-equilibrium alloying techniques such as ion implantation [12,13], sputter deposition [14–16], electrodeposition [17,18] equal channel angular pressing (ECAP) [19,20], high-pressure torsion (HPT) [21], and mechanical alloying [22–24] have been used to produce Al alloys with refined grain size and high solid solubility of the alloying elements. Mechanical alloying using a high-energy ball mill has been reported to provide extended solid solubility at room temperature along with the nanocrystalline structure that results in improved mechanical properties [10,25,26], high thermal stability [27], and high corrosion resistance [6]. The alloys produced by ball milling are in the powder form which can be used for repairing or coating using the cold spray, additive manufacturing, and consolidation to produce net-shaped components by employing conventional powder metallurgical techniques such as cold compaction followed by sintering, hot pressing, hot isostatic pressing and spark plasma sintering, which have been reviewed recently [8].

Consolidation of ball-milled powders requires exposure to high temperatures which could cause grain growth and decomposition of supersaturated solid solution (SSS) to thermodynamically stable phases. Grain size can be controlled by several techniques, including but not limited to introducing secondary phase particles and

* Corresponding author.
E-mail address: rkgupta2@ncsu.edu (R.K. Gupta).

https://doi.org/10.1016/j.jmst.2022.02.008
1005-0302/

stabilizing grain boundaries. The introduction of borides such as NbB_2, VB_2, TiB_2 as grain refiners is one of the methods of achieving grain refinement and maintaining it during processing and service conditions [28–30]. Grain refiners are introduced during casting to achieve better mechanical properties, reduce porosity and hot tearing [31]. Whereas grain size in ball-milled alloys is refined and the challenge lies in retaining it during processing. Additionally, ball-milled alloys with high solid solubility of alloying elements are not in an equilibrium state and therefore possess a natural tendency of decomposing to stable phases if adequate activation energy is provided [32,33]. For example, the equilibrium solid solubility of V in Al at 25 °C is 5.22×10^{-7} at.% [34] whereas ball-milled Al-5 V alloy has 2.93 at.% V in solid solution, which contains high driving force to achieve equilibrium state comprising of Al and Al-V intermetallics. Therefore, an appropriate choice of consolidation technique and processing parameters is deemed essential to retain the ball-milled microstructure and properties. For instance, hot isostatic pressing (HIP) requires a high temperature and a long time to improve the density of the material which causes significant grain growth and formation of thermodynamically stable phases [35,36]. Spark plasma sintering (SPS) results in dense materials in a short time by reducing the inter-particle distance through Joule's heating. SPS is a novel tool for processing alloys and composites at lower temperatures than conventional processing routes [9,37–39]. For instance, Esteves et al. produced nanocrystalline AA5083 with high solid solubility of V using SPS [9,39]. High heating rate (up to 1000 K/min) and low holding times are attributed to restrict grain growth during the SPS [40]. The microstructure of the spark plasma sintered (SPSed) alloys depends on the SPS temperature.

Alloying of Al with corrosion-resistant alloying elements (V, Cr, Mo, Ni, Ti, Nb) using HEBM has been shown to enhance the corrosion resistance and mechanical properties [7,9,41]. Among corrosion-resistant alloying elements, V has been most effective due to its efficiency in increasing corrosion resistance and strength, high thermal stability, and relatively lower density. However, the hardness, elastic modulus, and microstructural evolution of Al-V alloys during the consolidation process have not been studied. This work presents the influence of the SPS temperature on the Al-*x*V alloys which were produced by HEBM in the form of supersaturated solid solution. The solid solubility of V in Al, formation of secondary phases, and grain growth after various SPS temperatures were studied using X-ray diffraction, scanning electron microscope and transmission electron microscope.

2. Experimental procedure

2.1. Powder preparation and consolidation

Al-*x*V alloys (where $x = 2$ at.%, 5 at.%, and 10 at.%) were produced by HEBM of elemental powders in high purity Ar atmosphere where oxygen content was kept < 25 ppm. The aluminum powder having 99.7% purity with a mesh size of −50/+100, and vanadium powder (99.8% pure) of ∼100 mesh size were added to hardened stainless steel jars containing hardened stainless steel balls. The total weight of the Al and V powder was 25 g, and the ball-to-powder weight ratio was kept 16:1. Stearic acid was used as process control agent (PCA) to reduce cold welding and agglomeration of the metallic powders. Amount of stearic acid was kept 1.5 wt.% of the metal powder. HEBM was performed using a planetary ball mill at a speed of 280 r/min. Milling times for Al-2V, Al-5V, and Al-10V were 100, 40, and 40 h, respectively. Maximum achievable solid solubility at a given milling speed has been shown to depend on the alloy composition and milling time in Ref [42]., and therefore, the milling times were selected to achieve the highest solid solubility. The milling was paused for 30 min after every 1 h to avoid excessive heating.

The jars after milling were opened in the Ar atmosphere and the Al-*x*V alloy powder were consolidated by two methods: (1) compaction in a tungsten carbide die at room temperature using uniaxial pressure of 3 GPa, and (2) SPS with a dwell time of 5 min. SPS was performed at 200, 250, 300, and 400 °C. 1 GPa pressure was used for SPS at 200, 250, and 300 °C whereas 600 MPa was used for SPS at 400 °C. SPS was performed using SPS 10–3 thermal technology LLC. Punches and dies of tungsten carbide along with the graphite foil were used to obtain the sample of 10 mm diameter and 4 mm thickness. The SPS was conducted in Ar atmosphere. A heating rate of 50 °C/min was employed and the temperature was controlled using a thermocouple. The alloy produced by compaction at room temperature was termed cold compacted (CC). A high consolidation pressure of 3 GPa at room temperature was used due to the high hardness of HEBM Al alloy powder.

2.2. Nanoindentation

Hardness and elastic modulus of different regions were obtained from nanoindentation using Bruker Hysitron TI 980. The load of 1000 μN with a dwell time of 10 s was applied to indent the specimens.

2.3. Characterization techniques

Field emission scanning electron microscopy (FE-SEM) study was carried out using Tescan Lyra 3 FIB-FESEM operated at 20 kV acceleration voltage. Secondary electron (SE) and backscattered electron (BSE) images along with energy-dispersive X-ray spectroscopy (EDXS) data were obtained to study the particle size, inter-particle boundaries, porosity, elemental distribution, and distribution of phases. Specimens were polished to 0.05 μm finish using diamond suspension and ultrasonicated for 5 min in ethanol to remove the residue of polishing media.

X-ray diffraction (XRD) study was conducted using Rigaku SmartLab X-ray diffractometer to analyze the phase identification, change in grain size and solid solubility. The characterization was performed using Cu $K\alpha$ radiation for a 2θ range of 15°−85°, the scan rate of 1°/min and 0.02° step size. Subsequently, the grain size was calculated by the Scherrer method [43] after disregarding the instrumental peak broadening with the help of the NIST standard silicon sample.

Scanning transmission electron microscopy (S/TEM) was performed using Talos F200X G2 on Al-10V alloy produced by cold compaction and spark plasma sintering at 400 °C. The specimens were prepared by the focus ion beam (FIB) technique to cut the cross-section of the specimen using the lift-out method mentioned in [44]. Before preparing the electron-transparent lamellae, the surface was protected by depositing the first layer of 200 nm platinum cap using electron beam and the second layer of 300 nm platinum using ion beam milling over the first layer. High-angle annular dark-field (HAADF) and bright-field (BF) images were acquired along with EDXS elemental mapping to obtain the elemental distribution.

3. Results

3.1. Particle size and size distribution of ball-milled Al-xV alloys

Secondary electron (SE) images of the HEBM Al-*x*V ($x = 2$ at.%, 5 at.%, and 10 at.%) alloy powder particles in as-milled conditions are shown in Fig. 1. The particle size distribution is presented below SEM images, which reveals that increasing V content decreases the particles size and particle size distribution. Observed refinement of particles with the increase in solute content is consistent with reported literature [8] and is attributed to increased embrittlement

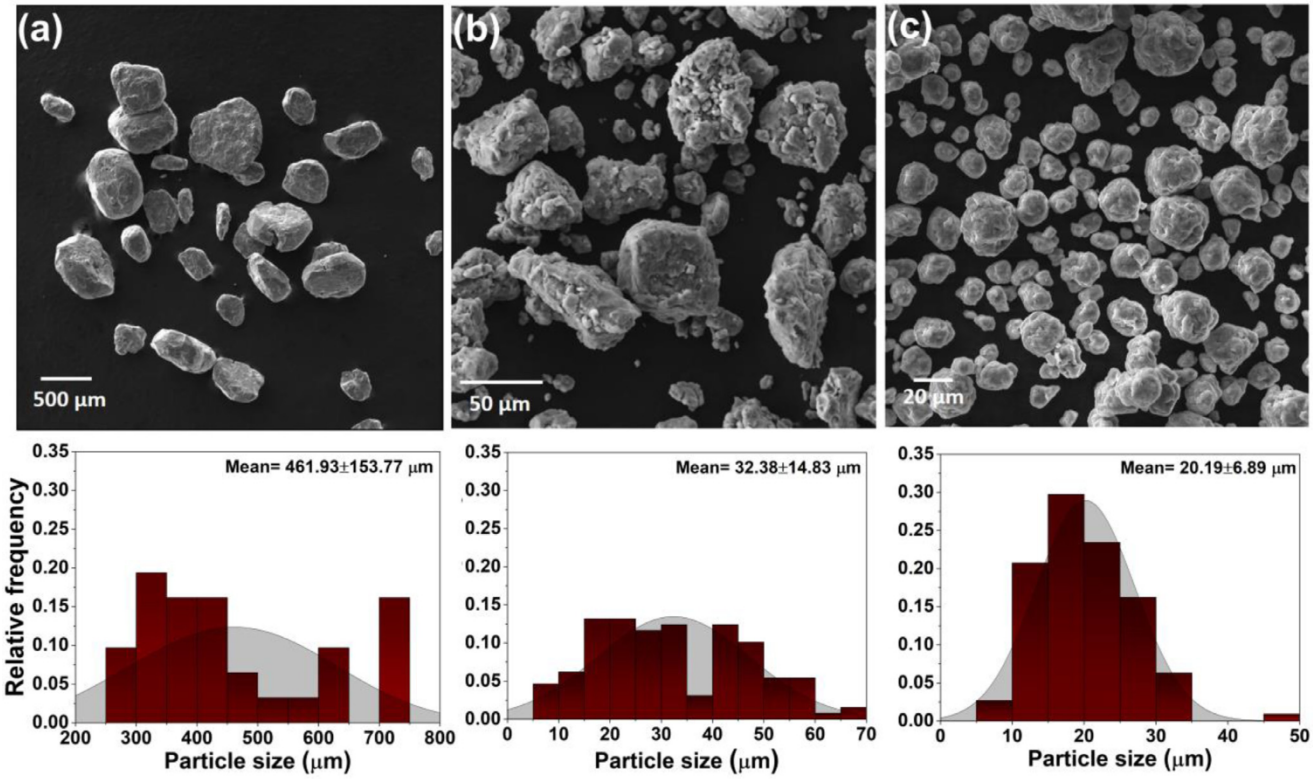

Fig. 1. SEM-SE images of high-energy ball-milled powder of (a) Al-2V, (b) Al-5V, and (c) Al-10V alloys with the particle size distribution graph at the bottom.

Table 1
Values for different parameters obtained after HEBM and subsequently consolidated by cold compaction (CC).

Alloy	Particle size (μm)	Solid solubility (at.%)	Grain size (nm)	Lattice parameter (Å)
Al-2V CC	462±154	1.8	33.6	4.0346
Al-5V CC	32±15	4.0	19.7	4.0176
Al-10 VCC	20±7	5.4	12.3	4.0066

of alloy with increasing V content. The average powder particle size is listed in Table 1.

3.2. Preliminary investigation for phase identification, grain size and solid solubility

The XRD peak for Al-*x*V alloys produced by cold compaction and SPS are presented in Fig. 2, which demonstrates the effect of SPS temperature on peak position and broadening. The peak positions of pure Al and Al_3V intermetallic are indicated with dotted vertical lines for reference. The Al peaks for cold compacted alloys appear at higher 2θ value indicating lower lattice parameter and higher V content in the solid solution (shown in Fig. 3(b)). The contraction of the lattice parameter is caused by the smaller effective atomic radius of V in Al-V solid solution i.e., 134.1 pm whereas the atomic radius of Al is 142 pm [45]. An increase in SPS temperature causes Al peaks to shift towards lower 2θ value and close to the 2θ of pure Al which indicate an increase in lattice parameter and decrease in solid solubility of V. At higher sintering temperature, i.e., 400 °C, the peak of Al_3V intermetallic began to emerge for all the compositions.

The grain size of Al-*x*V alloys is presented in Fig. 3(a). The average grain size for cold compacted alloys decreased with the increase in V content (Table 1) which is consistent with literature reporting the effect of solute on grain refinement [46–50]. For instance, in Al-Ti alloy, the addition of 5 wt.% Ti reduced the grain to 16 nm [49] while the addition of 35 at.% yielded to 10 nm [50]. Grain growth was observed in spark plasma sintered alloys. However, the average grain size was below 50 nm showing retention of nanocrystalline structure at all SPS temperatures.

The equilibrium solid solubility of V in Al at room temperature is 5.43×10^{-7} at.% [34] and therefore production of Al-V alloys using a conventional processing route such as casting results in coarse intermetallics. Non-equilibrium processing techniques such as HEBM has been reported to result in high solid solubility of V where the solid solubility was calculated using Vegard's law as mentioned in Refs [7,42]. and provided in Supplementary file Fig. 3.(b) shows the solid solubility of V of each composition concerning sintering temperature. A significant enhancement in solid solubility of V was achieved after the HEBM and is listed in Table 1. The solid solubility of V increased with the increase in added V while the ratio of solid solubility to added solute decreased. This indicates the increase in unalloyed V or intermetallics phases with increasing V content in the alloy. As the SPS temperature increased, the solid solubility of V decreased gradually indicating the decomposition of the supersaturated solid solution to Al and Al-V intermetallics. Nonetheless, the solid solubility of the V for all SPS temperatures was significantly higher than the equilibrium solid solubility of V in Al at room temperature.

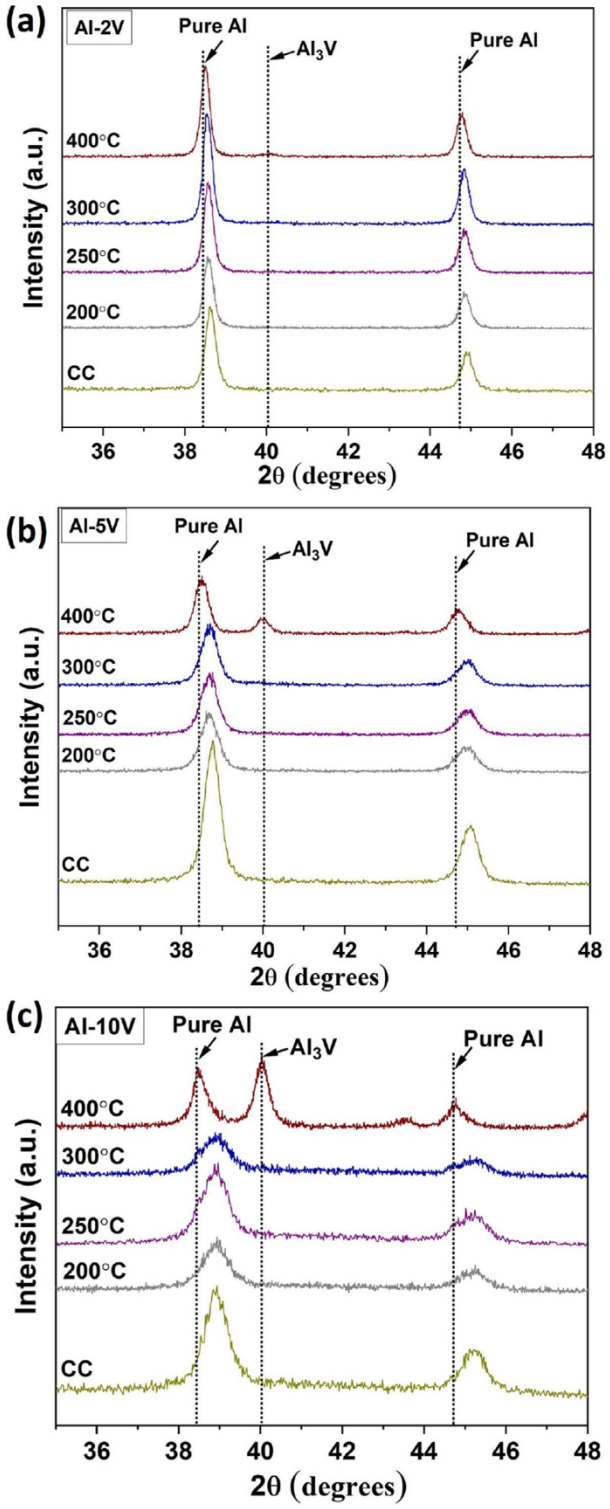

Fig. 2. XRD profiles of (a) Al-2V, (b) Al-5V, and (c) Al-10V showing the shift in peaks and formation of intermetallic as a function of SPS temperature. The dotted lines represent the position of the peak for pure Al and Al_3V for reference to observe the peak shift.

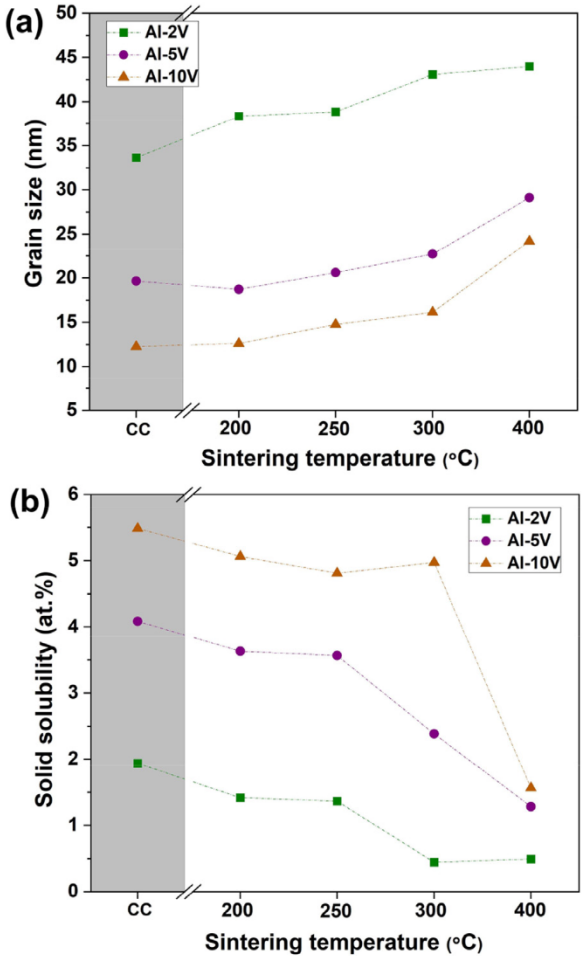

Fig. 3. (a) Grain size, and (b) solid solubility of V in Al as a function of SPS temperature. Data for the cold compacted alloy is alloy is also included for comparison.

3.3. Influence of sintering temperature on the microstructure

Fig. 4 shows the BSE images of the consolidated Al-*x*V alloys ranging from compaction at room temperature (CC) to SPS at 400 °C. The fine bright particles (denoted as red dotted circles) and coarse bright particles (indicated as blue arrows) were observed in the microstructure throughout all compositions. The EDXS analysis confirmed the fine bright particles (200–300 nm) to be unalloyed V particles while the coarse bright particles (500 nm–1 μm) to be the Fe-rich particles, which were introduced from the milling media during HEBM. The inter-particle boundaries and porosity were observed in cold compacted alloys, which increased in the order of Al-2V < Al-5V < Al-10V. The densification by ram displacement and the change in the material density are presented in Figs. S1 and S2 in the Supplementary Materials, respectively. During the SPS, higher ram displacement is observed with the increase in sintering temperature for all compositions. This indicates an increase in densification with the increase in sintering temperature. Whereas the ram displacement reduced with the increase in V content, which shows lower densification attributed to the increase in hardness and grain refinement. Porosity is also dependent on V content, which increased with the increase in hardness and grain refinement as a function of V content.

The inter-particle boundaries and pores began to diminish with the increase in sintering temperature for all the compositions (Fig. 4). In Al-5V, as the sintering temperature increased, a dark phase, shown by the yellow arrow, emerged at the inter-particle porosity with the size range of 2–7 μm. The volume fraction of this dark phase increased with the increase in sintering temperature (Fig. 4(e–h)). A similar phenomenon was observed in Al-10 V, where the dark appearing phase filled the inter-particle porosity (Fig. 4(i–l)). Additionally, a new bright streak-type phase at 400 °C (Fig. 4) appeared at the inter-particle boundaries and around the dark phase as denoted by the purple arrow. This bright streak-type

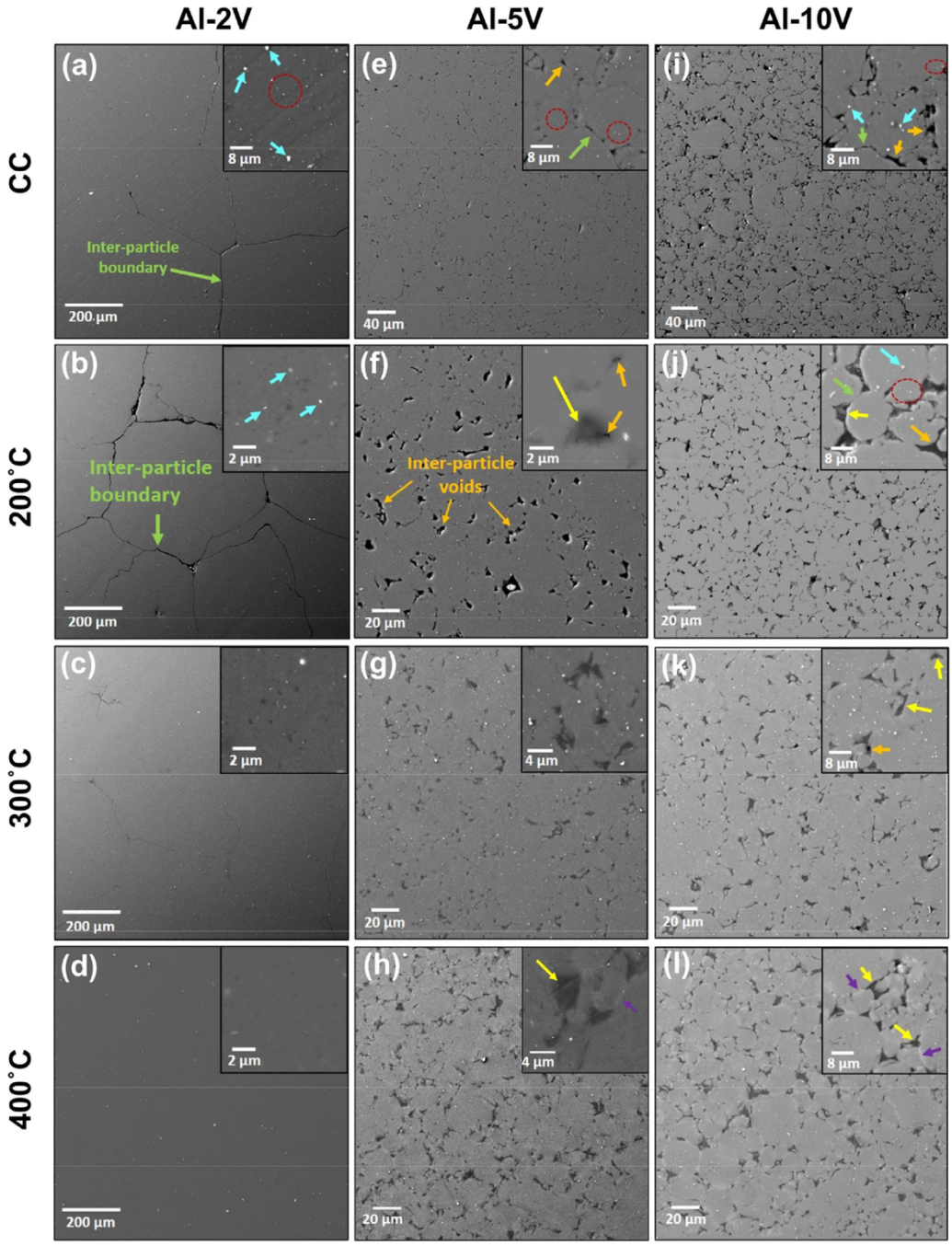

Fig. 4. BSE images of Al-2V (a-d), Al-5V (e-h), and Al-10V (i-l) after high-energy ball milling and consolidation at room temperature (CC) and SPS at 200, 250, 300, and 400 °C, respectively. 3 GPa pressure was applied for cold compaction. 1 GPa pressure was used for SPS at 200, 250, and 300 °C, while 600 MPa was used at 400 °C. High magnification images are shown as an inset on the top-right corner. The dark phase, bright steak-type phase, inter-particle boundaries, and inter-particle pores are indicated by yellow, purple, green, and orange arrows, respectively. Unalloyed V particles and abraded stainless steel particles are denoted by the dark red dotted circle and cyan arrow, respectively.

phase was also observed in Al-5 V alloy SPSed at 400 °C but was not as prominent. The thickness and intensity of the bright streak-type phase increased with increasing V content. SEM-EDXS analysis on the Al-10V alloy SPSed at 400 °C (Fig. 5) revealed that the dark phase was V-lean phase while the bright streak-type phase was V-rich phase. V-rich phase is appeared to contain Al_3V as detected from XRD and EDXS analysis revealed Al to V ratio of 3. With the increase in sintering temperature, the decomposition of supersaturated solid solution at the inter-particle boundary increased and can be observed in Figs. 4(l) and 5. The absence of Al_3V for SPS temperatures below 400 °C could be attributed to lower volume fraction. It should be noted that the decomposition of Al-V solid solution depends on SPS time and temperature, and decomposition kinetics is lower at lower temperatures.

S/TEM was performed on Al-10V produced by compaction at room temperature and SPS at 400 °C (Figs. 6 and 7). Homogeneous distribution of V along with unalloyed V as confirmed from EDXS mapping was observed in the cold compacted alloy (Fig. 6). TEM analysis shows fine grains with an average grain size of ~17 nm (Fig. S3) which is close to the grain size calculated by XRD. The STEM image of Al-10V SPSed at 400 °C (Fig. 7(a)) reveals bimodal grain size and presence of the V-lean phase, V-rich phase, and ma-

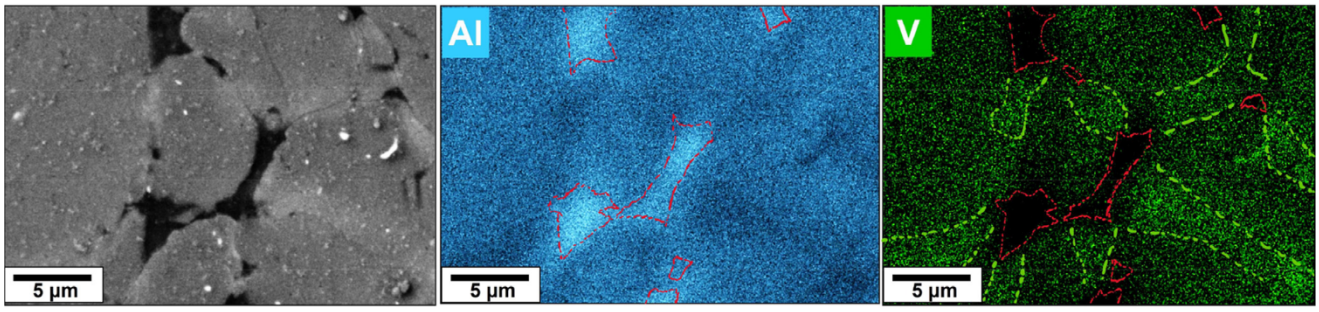

Fig. 5. EDXS area maps of Al and V for Al-10V SPSed at 400 °C. Red dotted lines show the V-lean phase; green dotted lines indicate the segregation of V (V-rich phase) along the inter-particle boundary.

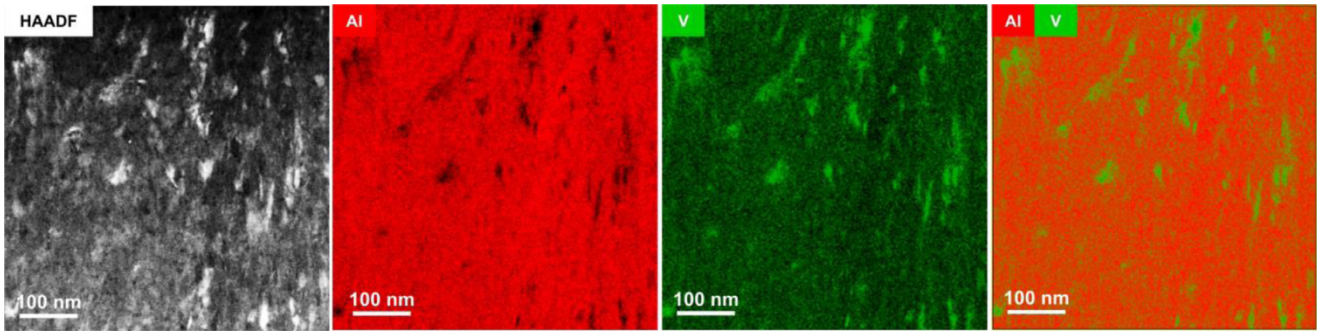

Fig. 6. HAADF image and STEM-EDXS area maps for cold compacted Al-10V alloy showing fine V-rich regions in the alloy.

trix. The V-lean phase consists of large grains with a size range of 400 nm-1 μm. The EDXS elemental mapping confirmed that these large grains consist of Al with V content varying from 0.1 to 1.5 at.%. While the V-rich region and matrix still exhibited nano-sized grains of 40.7 nm (Fig. S4), which is close to the grain size calculated using XRD. The STEM-HAADF image in Fig. 7(b) shows the magnified region comprising inter-particle boundaries, V-lean phase, and V-rich phase. Oxygen was revealed between the V-lean and V-rich phases, indicating the presence of inter-particle boundary as the particles are covered by a thin oxygen layer and also oxidation at inter-particle boundaries is plausible during SPS. Decomposition of the supersaturated solid solution of Al-V and microstructural evolutions appears to depend on the relative position from the inter-particle boundaries Fig. 7.(c–e) shows the typical high-resolution images of the matrix taken as a function of relative distance from the inter-particle boundary. A region close to the inter-particle boundary shows uniformly distributed fine bright particles which appear to be Al_3V (Fig. 7(c)). A cellular structure consisting of V as cell boundaries appears to emerge while moving away from the interparticle regions (Fig. 7(c–e)). S/TEM analysis indicates complex microstructure and heterogenous distribution of V at the nanoscale in the matrix of Al-10V alloys SPSed at 400 °C.

3.4. Change in hardness and elastic modulus

Nanoindentation was conducted to investigate the evolution of hardness and the elastic modulus (E) with SPS temperature (Table 2). Additionally, hardness and E of pure Al and commonly used commercial Al alloys also are listed in Table 3 for comparison. Pure Al exhibited a hardness of 0.6 GPa and E of 71 GPa (Table 3). The hardness and elastic modulus of the Al-xV alloy were significantly higher than commercial alloys and a strong function of V content and SPS temperature. Elastic modulus has increased with the increase in V content. E is a strong function of solid solubility of the V and lattice parameter. A decrease in solid solubility with increasing SPS temperature resulted in decreased E for the Al-xV alloys. V-lean phase showed the lowest E due to the low V content. V-rich phase which consists of Al_3V showed the highest E. Applications of aluminum alloys are limited in the fields requiring high stiffness due to the lower elastic modulus. High stiffness of Al alloys shown here demonstrates a method of designing Al alloys by increasing the solid solubility of the appropriate alloying elements. Further research is required for developing a fundamental understanding and forming a theoretical framework.

Al-2V alloy showed single-phase matrix (Fig. 4(a–d)) where hardness decreased with increasing SPS temperature. Al-5V and Al-10V alloys showed the presence of V-lean and V-rich phases in addition to the matrix (Fig. 4(e–l)). The hardness of the matrix and V-lean phase decreased with increasing SPS temperature. Generally, the hardness increases with the reduction in the porosity [51]. However, the trend is not observed over here. For instance, Al-10V showed maximum porosity due to high grain refinement and it is expected that the hardness would increase with the decrease in porosity as a function of sintering temperature. Therefore, the synergic effect of grain growth and loss of solid solubility were more prominent than the porosity effect in supersaturated solid solution Al-V alloy. The hardness of the V-rich phase was more than that of the matrix due to the presence of Al_3V and high V content. The complex microstructure, hardness, and elastic modulus of various phases are interesting, and a precise mechanistic understanding would require focused research efforts.

4. Discussion

Spark plasma sintering of Al-V alloy formed a complex microstructure, which was dependent on both V content and SPS temperature. These ball-milled Al-V alloys exhibited high solid solubility of V in Al–six orders of magnitude higher than predicted from the phase diagram. Therefore, alloys are not in equilibrium state and depict high driving force for the decomposition. Alloys need adequate activation energy to decompose. The activation energy is provided by exposing alloys to SPS temperatures. Kinetics of

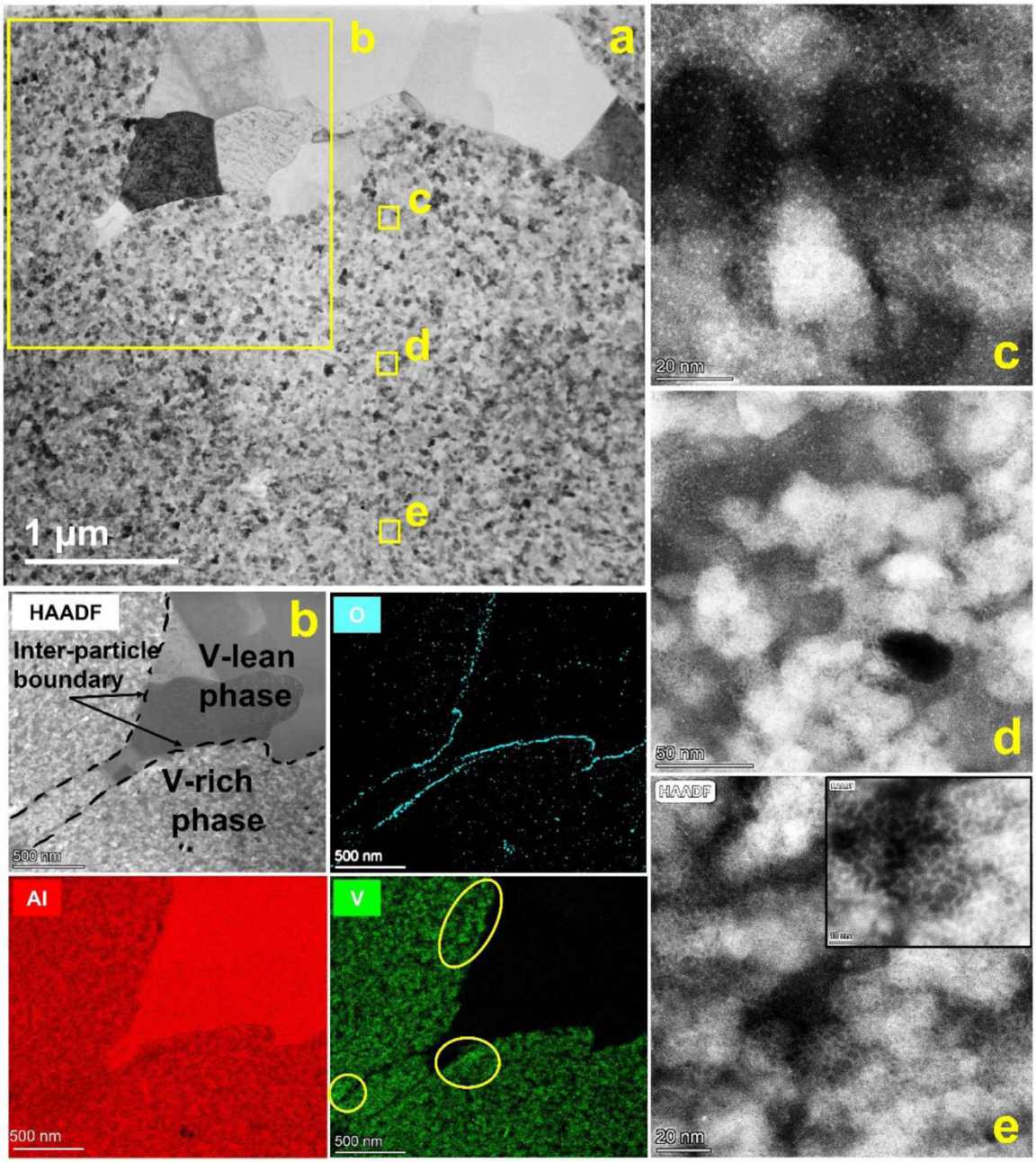

Fig. 7. (a) STEM-BF image of Al-10V alloy (SPSed at 400 °C) showing regions with fine grains (and V-rich) and coarse grains (V-lean). (b) High-resolution HAADF image and EDXS area maps for V, Al, and O. The yellow circles in V-EDXS area maps represent the V-rich phase along the V-rich and V-lean interface, (c) HAADF-STEM image showing the fine bright particles of Al_3V at the vicinity of the V-lean phase, (d) HAADF-STEM image showing the combination of bright particles and network structure of V (e) HAADF-STEM image taken far from the V-lean phase (i.e., close to particle center) showing the network structure of V.

decomposition would depend on SPS temperature–higher the temperature, faster the decomposition. Therefore, high solid solubility of V was retained at lower temperatures. The schematic representation of the consolidation process and microstructural evolution occurring during the SPS process is presented in Fig. 8 to illustrate two concurrent phenomena of SPS: (1) when the particles come sufficiently close, localized melting (neck formation) between the particles occurs due to Joule's heating, and (2) microstructural evolution within powder particles and at the surface of particles occurs during the sintering process. V-rich and V-lean phases at the inter-particle boundary began to emerge due to the high temperature generated at the particle surface. The electrical current density flowing through the neck (particle surface) is higher than the particle center [52]. Therefore, the temperature gradient is generated from high to low while moving from the surface to the center, resulting in rapid neck growth and faster sintering at each particle surface. Such exposure to high temperature experienced by each particle surface leads to the decomposition of the supersaturated solid solution at that region. The localized melting at the surface caused the formation of coarse Al grains and Al-V intermetallics. The lower melting point of Al leads to the flow of Al to fill the inter-particle porosity. Additionally, low strength and high ductility of aluminum facilitates to accommodate the inter-particle porosity during SPS. The decomposition of supersaturated solid solution depends on the SPS temperature as well as time and it is expected to begin as soon as the activation energy through SPS temperature

Table 2
Hardness and elastic modulus of Al-xV obtained from nanoindentation at various region for different sintering temperatures.

Alloy	Sintering temp. (°C)	Indent position	Hardness (GPa)	Elastic modulus (GPa)
Al-2V	200	Matrix	2.43±0.11	88.14±2.79
	250	Matrix	2.40±0.06	87.26±1.85
	300	Matrix	2.11±0.14	86.68±2.72
	400	Matrix	1.94±0.04	82.03±2.48
Al-5V	200	Matrix	5.21±0.36	96.21±2.47
	250	Matrix	4.17±0.16	94.14±2.61
		V-lean phase	3.99±0.04	87.10±1.65
	300	Matrix	3.17±0.29	91.96±1.79
		V-lean phase	2.82±0.19	85.97±1.26
	400	Matrix	2.35±0.33	88.11±2.55
		V-lean phase	2.15±0.40	84.45±1.82
		V-rich phase	2.85±0.25	89.87±1.56
Al-10V	200	Matrix	6.24±0.23	108.53±3.62
	250	Matrix	5.56±0.24	104.54±3.59
	300	Matrix	4.73±0.18	100.98±2.10
		V-lean phase	2.76±0.23	87.60±1.26
	400	Matrix	3.09±0.44	98.01±3.56
		V-lean phase	2.61±0.40	87.01±2.98
		V-rich phase	4.24±0.62	111.72±4.66

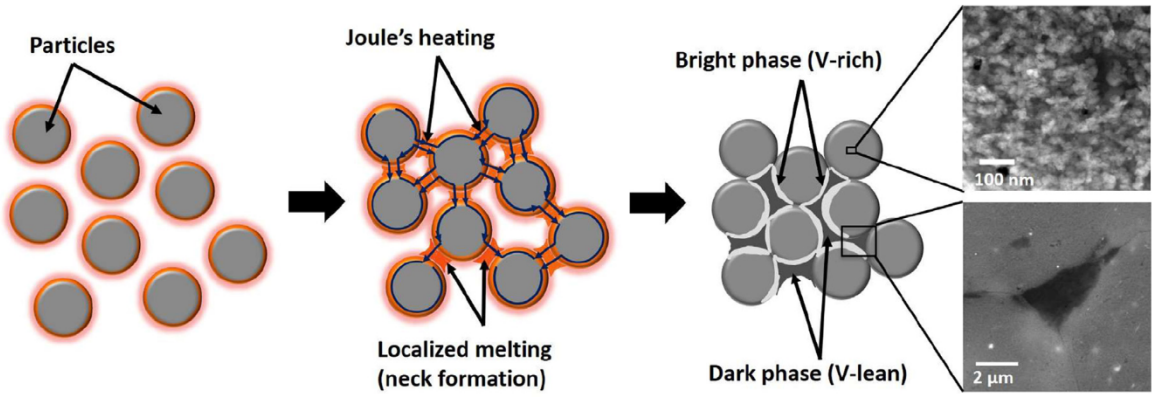

Fig. 8. Schematic diagram to illustrate the consolidation of HEBM powder particles and the microstructural evolution occurring during the SPS process.

Table 3
Hardness and elastic modulus of commercial Al alloys obtained from nanoindentation.

Commercial Alloy	Hardness (GPa)	Elastic Modulus (GPa)
Pure Al	0.60±0.12	71.09±4.63
AA2024-T3	2.00±0.12	76.06±2.91
AA5083-H116	1.31±0.04	75.34±1.36
AA7075-T651	2.23±0.13	72.28±1.98

was introduced. The formation of equilibrium phases is not clearly visible after SPS at 200 and 300 °C due to the lower volume fraction. While SPS at 400 °C led to the formation of V lean, V rich, and intermetallics (Fig. 4) Fig. 7.(c–e) shows the transition in the distribution of V as a function of distance from the inter-particle boundary. Such complex structure was not observed in cold compacted alloy but evolved due to the development of local thermal gradient during SPS.

5. Conclusions

The microstructure, hardness, and elastic modulus of Al-*x*V alloys produced by SPS were investigated and the main conclusions are as follows.

(1) High-energy ball milling and subsequent compaction at room temperatures were effective in producing Al-*x*V alloys with high solid solubility of V and grain size < 50 nm. The solid solubility of V increased with increasing V content in the alloy and was six orders of magnitude higher than the equilibrium value for Al-*x*V alloys.

(2) The refinement of particles and grains increased with the increase in solute concentration. The particle size reduced from ~462 μm in Al-2V to ~20 μm in Al-10V. Likewise, the grain size reduced from 34 nm in Al-2V alloy to 12 nm in Al-10V alloy.

(3) Spark plasma sintering at all temperatures was able to retain the average grain size below 50 nm. The microstructure was a strong function of SPS temperature and V content of the alloy. An increase in SPS temperature decreased the pores and solid solubility of V which caused the development of heterogeneous microstructure by decomposition of Al-V supersaturated solid solution. V-lean and V-rich phases began to emerge with the increase in SPS temperature.

(4) Microstructural evolution was corelated with the SPS process. The surface of particles experienced high temperature due to extreme electric current density at the surface compared to the particle center. Such phenomena resulted in the formation of the V-lean phase and V-rich phase. S/TEM analysis showed the bimodal grain size and heterogenous V distribution.

(5) Nanoindentation was used to measure hardness and elastic modulus, which were dependent on SPS temperature and composition. Increasing in V content and SPS temperature caused heterogeneous microstructure and the effect was observed in elastic modulus and hardness. Nonetheless, the hardness and

elastic modulus of Al-*x*V alloys presented herein were significantly higher than commercial Al alloys.

Acknowledgments

The authors would like to acknowledge the financial support received from the National Science Foundation (Nos. NSF-CMMI 1760204 and 2131440) under the direction of Dr. Alexis Lewis and would also like to thank for the XRD facility provided by National Polymer Innovation Center (NPIC), University of Akron. The TEM work was performed at the Analytical Instrumentation Facility (AIF) at North Carolina State University, which is supported by the State of North Carolina and the National Science Foundation (No. ECCS-1542015). This work made use of instrumentation at AIF acquired with support from the National Science Foundation (DMR-1726294).

Supplementary materials

Supplementary material associated with this article can be found, in the online version, at doi:10.1016/j.jmst.2022.02.008.

References

[1] M. Nakai, T. Eto, Mater. Sci. Eng. A 285 (2000) 62–68.
[2] W.S. Miller, L. Zhuang, J. Bottema, A.J. Wittebrood, P. de Smet, A. Haszler, A. Vieregge, Mater. Sci. Eng. A 280 (2000) 37–49.
[3] R.K. Gupta, A. Deschamps, M.K. Cavanaugh, S.P. Lynch, N. Birbilis, J. Electrochem. Soc. 159 (2012) C492–C502.
[4] K.D. Ralston, N. Birbilis, M. Weyland, C.R. Hutchinson, Acta Mater 58 (2010) 5941–5948.
[5] J.R. Davis, Corrosion of Aluminum and Aluminum Alloys, ASM International, 1999.
[6] R.K. Gupta, D. Fabijanic, R. Zhang, N. Birbilis, Corros. Sci. 98 (2015) 643–650.
[7] J. Esquivel, H.A. Murdoch, K.A. Darling, R.K. Gupta, Mater. Res. Lett. 6 (2018) 79–83.
[8] R.K. Gupta, B.S. Murty, N. Birbilis, An Overview of High-Energy Ball Milled Nanocrystalline Aluminum Alloys, Springer, 2017.
[9] L. Esteves, J. Christudasjustus, S.P. O'Brien, C.S. Witharamage, A.A. Darwish, G. Walunj, P. Stack, T. Borkar, R.E. Akans, R.K. Gupta, Corros. Sci. 186 (2021) 109465.
[10] C.S. Witharamage, J. Christudasjustus, J. Smith, W. Gao, R.K. Gupta, Npj Materials Degradation 6 (2022) 1–9.
[11] J. Esquivel, R.K. Gupta, Acta Metall. Sin. (Engl. Lett.) 30 (2017) 333–341.
[12] P.M. Natishan, E. McCafferty, G.K. Hubler, J. Electrochem. Soc. 135 (1988) 321–327.
[13] S. Venkatraman, M.R. Nair, D.C. Kothari, K.B. Lal, R. Raman, Nucl. Instrum. Methods Phys. Res. 19 (1987) 241–246.
[14] G.S. Franke, X.B. Chen, R.K. Gupta, S. Kandasamy, N. Birbilis, J. Electrochem. Soc. 161 (2014) C195.
[15] P.J. Kelly, R.D. Arnell, Vacuum 56 (2000) 159–172.
[16] G.S. Frankel, M.A. Russak, C. v Jahnes, M. Mirzamaani, V.A. Brusic, J. Electrochem. Soc. 136 (1989) 1243–1244.
[17] T. Tsuda, C.L. Hussey, G.R. Stafford, J. Electrochem. Soc. 151 (2004) C379–C384.
[18] T. Tsuda, C.L. Hussey, J. Min. Metall. 39 (2003) 3–22.
[19] M. Hoseini, A. Shahryari, S. Omanovic, J.A. Szpunar, Corros. Sci. 51 (2009) 3064–3067.
[20] D. Song, A. bin Ma, J. hua Jiang, P. hua Lin, D. hui Yang, Trans. Nonferr. Metals Soc. China (Engl. Ed.) 19 (2009) 1065–1070.
[21] W.T. Sun, X.G. Qiao, M.Y. Zheng, C. Xu, N. Gao, M.J. Starink, Mater. Des. 135 (2017) 366–376.
[22] K.M. Youssef, R.O. Scattergood, K.L. Murty, C.C. Koch, Scr. Mater. 54 (2006) 251–256.
[23] O.N. Senkov, F.H. Froes, V.v. Stolyarov, R.Z. Valiev, J. Liu, Nanostruct. Mater. 10 (1998) 691–698.
[24] M.U.F. Khan, A. Patil, J. Christudasjustus, T. Borkar, R.K. Gupta, J. Magnes. Alloy. 8 (2020) 319–328.
[25] T.T. Sasaki, T. Ohkubo, K. Hono, Acta Mater. 57 (2009) 3529–3538.
[26] J.A. Rodríguez, J.M. Gallardo, E.J. Herrera, J. Mater. Sci. 32 (1997) 3535–3539.
[27] V.L. Tellkamp, E.J. Lavernia, A. Melmed Metall. Mater. Trans. A 32 (2001) 2335–2343.
[28] J. Xu, R. Li, Q. Li, Metall. Mater. Trans. A 52 (2021) 1077–1094.
[29] Y. Li, Y. Jiang, B. Liu, Q. Luo, B. Hu, Q. Li, J. Mater. Sci. Technol. 65 (2021) 190–201.
[30] Y. Li, Y. Jiang, B. Hu, Q. Li, Scr. Mater. 187 (2020) 262–267.
[31] J. Xu, Y. Li, B. Hu, Y. Jiang, Q. Li, J. Mater. Sci. 54 (2019) 14561–14576.
[32] Q. Luo, Y. Guo, B. Liu, Y. Feng, J. Zhang, Q. Li, K. Chou, J. Mater. Sci. Technol. 44 (2020) 171–190.
[33] Q. Li, X. Lin, Q. Luo, Y. Chen, J. Wang, B. Jiang, F. Pan, Int. J. Miner. Metall. Mater. 29 (2022) 32–48.
[34] J. Esquivel, M.G. Wachowiak, S.P. O'Brien, R.K. Gupta, J. Alloy. Compd. 744 (2018) 651–657.
[35] J. Besson, M. Abouaf, Acta Metall. Mater. 39 (1991) 2225–2234.
[36] H.V. Atkinson, S. Davies, Metall. Mater. Trans. A 31 (2000) 2981–3000.
[37] G. Walunj, A. Bearden, A. Patil, T. Larimian, J. Christudasjustus, R.K. Gupta, T. Borkar, Materials 13 (2020) 5306 Basel.
[38] J. Ye, L. Ajdelsztajn, J.M. Schoenung, Metall. Mater. Trans. A 37 (2006) 2569–2579.
[39] L. Esteves, C.S. Witharamage, J. Christudasjustus, G. Walunj, S.P. O'Brien, S. Ryu, T. Borkar, R.E. Akans, R.K. Gupta, J. Alloy. Compd. 857 (2021) 158268.
[40] J. Trapp, B. Kieback, Powder Metall. 62 (2019) 297–306.
[41] J. Esquivel, R.K. Gupta, J. Alloy. Compd. 760 (2018) 63–70.
[42] C.S. Witharamage, J. Christudasjustus, R.K. Gupta, J. Mater. Eng. Perform. 30 (2021) 3144–3158.
[43] B.D. Cullity, Elements of X-Ray Diffraction, Addison-Wesley Publishing Company, Inc., Boston, 1956.
[44] S.P. O'Brien, J. Christudasjustus, L. Esteves, S. Vijayan, J.R. Jinschek, N. Birbilis, R.K. Gupta, NPJ Mater. Degrad. 5 (2021) 1–10.
[45] T. Uesugi, K. Higashi, Comput. Mater. Sci. 67 (2013) 1–10.
[46] D. Mukhopadhyay, C. Suryanarayana, F. Froes, Metall. Mater. Trans. A 26 (1995) 1939–1946.
[47] B. Srinivasarao, C. Suryanarayana, K. Oh-ishi, K. Hono, Mater. Sci. Eng. A 518 (2009) 100–107.
[48] A. Calka, W. Kaczmarek, J.S. Williams, J. Mater. Sci. 28 (1993) 15–18.
[49] J.H. Choi, K. Il Moon, J.K. Kim, Y.M. Oh, J.H. Suh, S.J. Kim, J. Alloy. Compd. 315 (2001) 178–186.
[50] G.J. Fan, W.N. Gao, M.X. Quan, Z.Q. Hu, Mater. Lett. 23 (1995) 33–37.
[51] A. Jahangiri, S.P.H. Marashi, M. Mohammadaliha, V. Ashofte, J. Mater, Process. Technol. 245 (2017) 1–6.
[52] N. Sharma, S.N. Alam, B.C. Ray, in: Spark Plasma Sintering of Materials, Springer International Publishing, Cham, 2019, pp. 21–59.